



Does Turbulence along the Coronal Current Sheet Drive Ion Cyclotron Waves?

Daniele Telloni¹, Gary P. Zank^{2,3}, Laxman Adhikari², Lingling Zhao², Roberto Susino¹, Ester Antonucci¹, Silvano Fineschi¹, Marco Stangalini⁴, Catia Grimani^{5,6}, Luca Sorriso-Valvo^{7,8}, Daniel Verscharen⁹, Raffaele Marino¹⁰, Silvio Giordano¹, Raffaella D'Amicis¹¹, Denise Perrone⁴, Francesco Carbone¹², Alessandro Liberatore¹³, Roberto Bruno¹¹, Gaetano Zimbardo¹⁴, Marco Romoli¹⁵, Vincenzo Andretta¹⁶, Vania Da Deppo¹⁷, Petr Heinzel^{18,19}, John D. Moses²⁰, Giampiero Naletto²¹, Gianalfredo Nicolini¹, Daniele Spadaro²², Luca Teriaca²³, Aleksandr Burtovoi²⁴, Yara De Leo^{23,25}, Giovanna Jerse²⁶, Federico Landini¹, Maurizio Pancrazzi¹, Clementina Sasso¹⁶, and Alessandra Slemmer¹⁷

¹ National Institute for Astrophysics, Astrophysical Observatory of Torino, Via Osservatorio 20, I-10025 Pino Torinese, Italy; daniele.telloni@inaf.it

² Center for Space Plasma and Aeronomic Research, University of Alabama in Huntsville, Huntsville, AL 35805, USA

³ Department of Space Science, University of Alabama in Huntsville, Huntsville, AL 35805, USA

⁴ Italian Space Agency, Via del Politecnico snc, I-00133 Roma, Italy

⁵ University of Urbino Carlo Bo, Department of Pure and Applied Sciences, Via Santa Chiara 27, I-61029 Urbino, Italy

⁶ National Institute for Nuclear Physics, Section in Florence, Via Bruno Rossi 1, I-50019 Sesto Fiorentino, Italy

⁷ National Research Council, Institute for the Science and Technology of Plasmas, Via Amendola 122/D, I-70126 Bari, Italy

⁸ Swedish Institute of Space Physics, Ångström Laboratory, Lägerhyddsvägen 1, SE-751 21 Uppsala, Sweden

⁹ Mullard Space Science Laboratory, University College London, Holmbury St. Mary, RH5 6NT Dorking, UK

¹⁰ Université de Lyon, Centre National de la Recherche Scientifique, École Centrale de Lyon, Institut National des Sciences Appliquées de Lyon, Université Claude Bernard Lyon 1, Laboratoire de Mécanique des Fluides et d'Acoustique, F-69134 Écully, France

¹¹ National Institute for Astrophysics, Institute for Space Astrophysics and Planetology, Via del Fosso del Cavaliere 100, I-00133 Roma, Italy

¹² National Research Council, Institute of Atmospheric Pollution Research, c/o University of Calabria, I-87036 Rende, Italy

¹³ Jet Propulsion Laboratory, California Institute of Technology, Pasadena, CA 91109, USA

¹⁴ University of Calabria, Department of Physics, Ponte Pietro Bucci Cubo 31C, I-87036 Rende, Italy

¹⁵ University of Florence, Department of Physics and Astronomy, Via Giovanni Sansone 1, I-50019 Sesto Fiorentino, Italy

¹⁶ National Institute for Astrophysics, Astronomical Observatory of Capodimonte, Salita Moiariello 16, I-80131 Napoli, Italy

¹⁷ National Research Council, Institute for Photonics and Nanotechnologies, Via Trasea 7, I-35131 Padova, Italy

¹⁸ Czech Academy of Sciences, Astronomical Institute, Fričova 298, CZ-25165 Ondřejov, Czechia

¹⁹ University of Wrocław, Centre of Scientific Excellence Solar and Stellar Activity, ul. Kopernika 11, PL-51-622 Wrocław, Poland

²⁰ National Aeronautics and Space Administration, Headquarters, Washington, DC 20546, USA

²¹ University of Padua, Department of Physics and Astronomy, Via Francesco Marzolo 8, I-35131 Padova, Italy

²² National Institute for Astrophysics, Astrophysical Observatory of Catania, Via Santa Sofia 78, I-95123 Catania, Italy

²³ Max Planck Institute for Solar System Research, Justus-von-Liebig-Weg 3, D-37077 Göttingen, Germany

²⁴ National Institute for Astrophysics, Astrophysical Observatory of Arcetri, Largo Enrico Fermi 5, I-50125 Firenze, Italy

²⁵ University of Catania, Department of Physics and Astronomy, Via Santa Sofia 64, I-95123 Catania, Italy

²⁶ National Institute for Astrophysics, Astronomical Observatory of Trieste, Località Basovizza 302, I-34149 Trieste, Italy

Received 2022 December 8; revised 2023 January 19; accepted 2023 January 23; published 2023 February 28

Abstract

Evidence for the presence of ion cyclotron waves (ICWs), driven by turbulence, at the boundaries of the current sheet is reported in this paper. By exploiting the full potential of the joint observations performed by Parker Solar Probe and the Metis coronagraph on board Solar Orbiter, local measurements of the solar wind can be linked with the large-scale structures of the solar corona. The results suggest that the dynamics of the current sheet layers generates turbulence, which in turn creates a sufficiently strong temperature anisotropy to make the solar-wind plasma unstable to anisotropy-driven instabilities such as the Alfvén ion cyclotron, mirror-mode, and firehose instabilities. The study of the polarization state of high-frequency magnetic fluctuations reveals that ICWs are indeed present along the current sheet, thus linking the magnetic topology of the remotely imaged coronal source regions with the wave bursts observed in situ. The present results may allow improvement of state-of-the-art models based on the ion cyclotron mechanism, providing new insights into the processes involved in coronal heating.

Unified Astronomy Thesaurus concepts: [Magnetohydrodynamics \(1964\)](#); [Interplanetary turbulence \(830\)](#); [Alfvén waves \(23\)](#); [Solar corona \(1483\)](#); [Solar coronal heating \(1989\)](#); [Coronagraphic imaging \(313\)](#); [Solar wind \(1534\)](#); [Heliosphere \(711\)](#); [Space plasmas \(1544\)](#)

1. Introduction

The physical processes that heat the solar corona plasma to temperatures exceeding one million degrees, thereby driving the solar wind (Hundhausen 1972), are still strongly debated.

Solving this puzzle of the solar physics is central to the Parker Solar Probe (PSP; Fox et al. 2016) and Solar Orbiter (SO; Müller et al. 2020) missions. The many models proposed so far to explain the so-called “coronal heating problem” can be classified into two major categories, namely alternating current (AC) and direct current (DC) heating mechanisms. AC/DC models involve energy release by waves/turbulence or magnetic reconnection events (as nanoflares, Parker 1972) respectively. Reviews can be found in Zirker (1993) and

 Original content from this work may be used under the terms of the [Creative Commons Attribution 4.0 licence](#). Any further distribution of this work must maintain attribution to the author(s) and the title of the work, journal citation and DOI.

Mandrini et al. (2000). On the AC (wave/turbulence) side, two key mechanism candidates are ion cyclotron waves (ICWs) dissipation (Li et al. 1999; Cranmer 2000; Leamon et al. 2000; Hollweg & Isenberg 2002) and low-frequency magnetohydrodynamic (MHD) turbulence dissipation. The latter can further take place either through nonlinear coupling of a dominant outward Alfvén wave flux with a minority of inwardly reflected modes (Matthaeus et al. 1999; Verdini et al. 2009, 2010), or, in the Nearly Incompressible (NI) MHD theory, in the frame of quasi-2D turbulence dynamics generated by the magnetic carpet and advected into the solar corona where it can then dissipate (Zank et al. 2017, 2018, 2020). Although recent observational indications seem to point toward the interpretation in terms of the quasi-2D scenario (the reader is referred to Zank et al. 2021, where the above turbulence models are reviewed and their predictions tested against PSP observations), there is still no general consensus on which physical processes drive the deposition of the energy at small scales, needed to heat the plasma and accelerate the solar wind. Common to the aforementioned AC classifications, and indeed integral to energy transport and solar corona heating, are the collisionless field–particle interactions occurring at scales close to the proton inertial length and proton gyro-radius. At these scales, the solar wind, which has a fluid-like behavior in the inertial range of turbulence (see the exhaustive review by Bruno & Carbone 2013 and references therein), takes on dispersive kinetic characteristics (Bale et al. 2005; Howes et al. 2008; Sahraoui et al. 2010; Alexandrova et al. 2013). Energy is thus transferred from the fluctuating fields to thermal particle energy, that is, dissipated, resulting in plasma heating.

PSP measurements compare remarkably well with the quasi-2D turbulence model developed by Zank et al. (2017), both in slow (Adhikari et al. 2020b; Telloni et al. 2022b) and fast (Adhikari et al. 2020a, 2021) solar wind flows. In addition, the theoretical predictions based on the NI MHD theory do satisfactorily match the observed acceleration of coronal outflows to supersonic (Telloni et al. 2007a, 2007b) and super-Alfvénic (Adhikari et al. 2022) speeds. Succeeding in reproducing observations of both coronal and heliospheric plasmas, the NI quasi-2D model is thus gaining a reputation as a credible mechanism for solar wind plasma heating and acceleration. On the other hand, a number of fundamental major issues concerning the ion cyclotron heating mechanism (see Zank et al. 2021 for more details) seem to rule it out from playing a relevant role in the interplanetary space plasma-heating processes. A decade of remote-sensing observations of the extended corona with the ultraviolet coronagraph spectrometer (UVCS; Kohl et al. 1995) on board the Solar and Heliospheric Observatory (Domingo et al. 1995), however, appear to agree well with a scenario in which ions/atoms are heated by cyclotron-resonant interaction with high-frequency Alfvén waves (Kohl et al. 1998; Cranmer et al. 1999b). In particular, the kinetic temperatures of different coronal ion species were found to vary with their charge-to-mass Z/A ratio (Cranmer et al. 1999a), as expected for ICW dissipation, whose rate depends on the local ion gyro-frequency $\Omega_i \propto Z/A$. Similarly, in situ measurements also strongly indicate that ICW damping is involved in the energy cascade (Leamon et al. 1998; Bruno & Trenchi 2014). Evidence for the presence of ICWs in space plasmas (He et al. 2011; Podesta & Gary 2011; Bruno & Telloni 2015; Telloni et al. 2015; Luo et al. 2022) when the temperature-anisotropy thresholds of the

cyclotron instability are exceeded (Bale et al. 2009; Telloni & Bruno 2016; Telloni et al. 2019; Woodham et al. 2019) points to ion cyclotron resonance as a viable energy-conversion mechanism in collisionless plasmas (Bowen et al. 2022). Alternative heating mechanisms include, for example, resonant Landau damping of kinetic Alfvén waves (Howes et al. 2018; Chen et al. 2019; Carbone et al. 2022), and stochastic perpendicular heating of ions resulting from the violation of the magnetic moment conservation induced by large-amplitude turbulent fluctuations at ion scales (Chandran et al. 2010; Martinovic et al. 2020). These mechanisms, however, are not discussed here.

In the attempt to reconcile the remote-sensing and in situ observations in a unified view of the heating of the coronal plasma and the subsequent acceleration of the solar wind, local measurements of the coronal regions are needed. At present, PSP has only occasionally entered the solar corona (Kasper et al. 2021; Bandyopadhyay et al. 2022; Zank et al. 2022; Zhao et al. 2022; Marino & Sorriso-Valvo 2023), although its progressively shrinking orbits will ensure that the spacecraft spends extended periods immersed in the coronal plasma. Even then, though, single-spacecraft measurements will provide only one-point information, precluding a clear understanding of how the global (magnetic) configuration of coronal sources affects local dynamics and turbulence properties in space plasmas. It appears thus that remote-sensing observations of large-scale source regions of the solar wind are of critical importance to conduct this type of investigations. Correspondingly, these alone offer only some general, though not conclusive, insights. It follows that exploiting the synergies between in situ measurements and remote-sensing observations and, in particular, the joint PSP–SO observations of the Sun and its environment, is the most viable approach to answer key questions concerning the coronal heating. Two companion papers by Telloni et al. (2021, 2022c) can be considered a first attempt to exploit observations of Metis (the coronagraph aboard SO; Antonucci et al. 2020b; Fineschi et al. 2020) in combination with in situ PSP measurements collected while in orbital quadrature, to link global and local properties of coronal flows and study their evolution in the transition from sub- to super-Alfvénic wind.

The first Metis observations, performed in 2020, imaged the solar corona in its quasi-dipolar magnetic configuration typical of the minimum activity phase out to $\sim 7 R_\odot$, thus allowing the extension of the study of the morphology and dynamics of the coronal current sheet (CS), which originates at the cusp of the equatorial streamers, beyond the region explored with UVCS and limited to a heliocentric distance of $5 R_\odot$ (see the review by Antonucci et al. 2020a). In the Metis observations, the initial coronal part of the heliospheric current sheet, separating opposite polarities of the coronal magnetic field, is clearly outlined by a slightly warped quasi-equatorial layer of denser and slower wind plasma that is undergoing a significant acceleration between 4 and $5 R_\odot$ (Antonucci et al. 2023). These first Metis observations show that the zone where the slow wind is observed in the corona, $\lesssim 30^\circ$ in latitude, is structured as follows: the slowest wind, observed in a layer $< 10^\circ$ wide in latitude and associated with the current sheet, is surrounded by steep velocity gradients, a few degrees wide in latitude, indicating a transition to slow wind flows characterized by higher velocity but lower acceleration relative to plasma directly embedded in the current sheet (Antonucci et al. 2023).

This paper presents evidence on the occurrence of ICWs in the coronal structures explored by PSP, taking advantage of the SO/Metis—PSP joint observations of 2021 mid-January. Specifically, the results show that when PSP flies through the layers of the heliospheric CS remotely imaged by Metis in its initial coronal stretch, turbulence increases significantly causing the plasma to depart more from an equilibrium state. A case of local PSP measurements along the CS, in which a proton cyclotron instability driven by temperature anisotropy generates ICWs, is shown in the present work. This combined observation, the first of its kind to be reported, represents a step forward in understanding how coronal large-scale structures drive and regulate small-scale fluctuations/waves in the space plasma. This paper first presents a description of the coordinated SO/Metis—PSP observations (Section 2), then the methodological approach implemented to link local measurements of the solar wind to remotely imaged coronal source regions (Section 3), the observation of the onset of ICWs along the turbulent CS (Section 4), and finally concluding remarks on the results presented (Section 5).

2. SO/Metis—PSP Joint Observations

From 2021 January 14 through January 17, Metis acquired, with 4 hr cadence, 23 images of the white-light solar corona in an annular field of view (FOV) from 3.5 to 6.3 R_{\odot} , which were calibrated in flight according to De Leo et al. (2023). Figure 1(a) shows the Carrington map (i.e., a synoptic chart displayed using Carrington coordinates) of the polarized Brightness (pB) at a distance of 5 R_{\odot} above the East limb of the Sun.

The coronal CS, namely the initial part of the heliospheric current sheet that is imaged at coronal level, is clearly visible in the Metis-based Carrington map around the solar equator as the densest structure. In particular, the dark orange level line at $2 \times 10^{-10} B/B_{\odot}$ (which helps to roughly outline the CS boundaries) shows the apparent presence of a double structure for longitudes less than $\sim 132^{\circ}$. As discussed in Telloni et al. (2021), this is due to two small CS warps extending up to $\sim \pm 10^{\circ}$ in latitude. Due to its retrograde motion relative to the Sun’s rotation, PSP flies through the plane of the sky (POS) observed by Metis twice (and later to the Metis observation, see Shi et al. 2021; Telloni et al. 2022c, for a more extensive discussion on the PSP orbital characteristics). The PSP back-projected trajectory on the pB Carrington map is shown in Figure 1(a) with magenta and lime lines, respectively, for the first and second crossing. PSP collected measurements around the CS, while moving away from the Sun from 0.11 to 0.24 au (Figure 1(b)). The apparent location of PSP with respect to the CS observed by Metis is shown in Figures 1(c)–(h): during its orbit, PSP moved in latitude and sampled different portions of the CS.

3. Linking PSP Measurements to Metis Observations of Coronal Sources

Local solar wind measurements of PSP can thereby be related to the coronal source structures imaged by Metis. Figure 2 shows some relevant PSP-based MHD quantities projected onto the Metis pB Carrington map in $1^{\circ}68$ -wide bins. Specifically, panels (a)–(d) display the direction of the interplanetary magnetic field (IMF), the proton plasma $\beta_{\parallel} = v_{\text{th}\parallel}^2/v_A^2$ (where $v_{\text{th}\parallel}$ and v_A are the parallel proton

thermal and Alfvén speeds, respectively), the magnetic-field turbulence amplitude $\delta B/\langle B \rangle = \sqrt{\langle |B(t) - \langle B \rangle|^2 \rangle} / \langle B \rangle$ (where $\langle \dots \rangle$ indicates time averaging over the typical fluid scale of 10 minutes²⁷), and the magnetic-field deflection $z = (1 - \cos \alpha)/2$ (where α is the angle between the local and mean magnetic fields, Dudok de Wit et al. 2020). Magnetic field and plasma data come from the fluxgate magnetometer and the top-hat electrostatic analyzer of the FIELDS (Bale et al. 2016) and Solar Wind Electrons Alphas and Protons (Kasper et al. 2016) instrument suites on board PSP, respectively.

PSP measurements of the IMF direction (Figure 2(a)) agree with the topological structure of the CS imaged by Metis. Specifically, the polarity reversal (which identifies the CS boundaries) occurs in the proximity of the dark orange level line that helps to outline the CS edges. Thus, it can be deduced from PSP observations that the spacecraft, initially outside of the CS (in blue), first entered the CS at Carrington longitude of about 126° (in red), and crossed the CS a second time, exiting it at Carrington longitude of about 119° . A schematic of the magnetic topology of the CS thus inferred is illustrated in Figure 2(a). At the double crossing of the CS (occurring at the “CS layers,” Figure 2(a)), the plasma β_{\parallel} increases by an order of magnitude compared with the region outside (Figure 2(b)). This is expected when considering that the current sheet layers (dominated by opposite parallel magnetic currents) are sites of magnetic reconnection events, likely related, e.g., to the tearing mode instability (Priest 1985; Verneta et al. 1994; Phan et al. 2022), which tends to form magnetic islands, i.e., small flux ropes, disconnecting from the CS (Zhao et al. 2021; Renville et al. 2022). At the CS boundaries, the magnetic-field turbulence also increases (Figure 2(c)), mostly due to the change in field direction, as indicated by the concurrent increase in the parameter z (Figure 2(d)). Recent analysis of PSP measurements shows that turbulence is typically reduced in the proximity of the heliospheric CS (see, e.g., Chen et al. 2021 and references therein). In particular, observations suggest that closer to the CS (i.e., for angular distance from the CS within $\simeq 4^{\circ}$) fluctuations are similar to non-Alfvénic, slow solar wind (with steeper and broader power-law spectra, smaller fluctuation amplitude), while they are closer to Alfvénic fast wind further away. Zhao et al. (2020, 2021) presented a detailed analysis of PSP data in the vicinity of the CS, identifying many magnetic islands, which they argue are consistent with non-Alfvénic turbulence. These are preferentially located in the vicinity of the CS. Shi et al. (2022) also report, exploiting MHD simulations complemented by analysis of in situ data at 1 au, the decrease in Alfvénicity of turbulence around the heliospheric CS. The present observations lie within the angular range considered as CS in Chen et al. (2021), and therefore show finer details of the turbulence structure in its boundaries. This result is consistent with the following scenario. At the CS, the solar wind is slower than typical of other coronal regions. Nevertheless, the regions along it (i.e., its edges) are characterized by faster (though still slow) coronal flows and lower wind acceleration. This is clearly shown by Antonucci et al. (2023). It follows that the CS layers might be sites of velocity shears. These are also implied by the magnetic-field configuration, the velocity being inversely correlated with the expansion factor, which is maximum at the CS. Velocity shears are known to generate turbulence (Stawarz et al. 2016;

²⁷ Note that the results are the same at other scales in the inertial range.

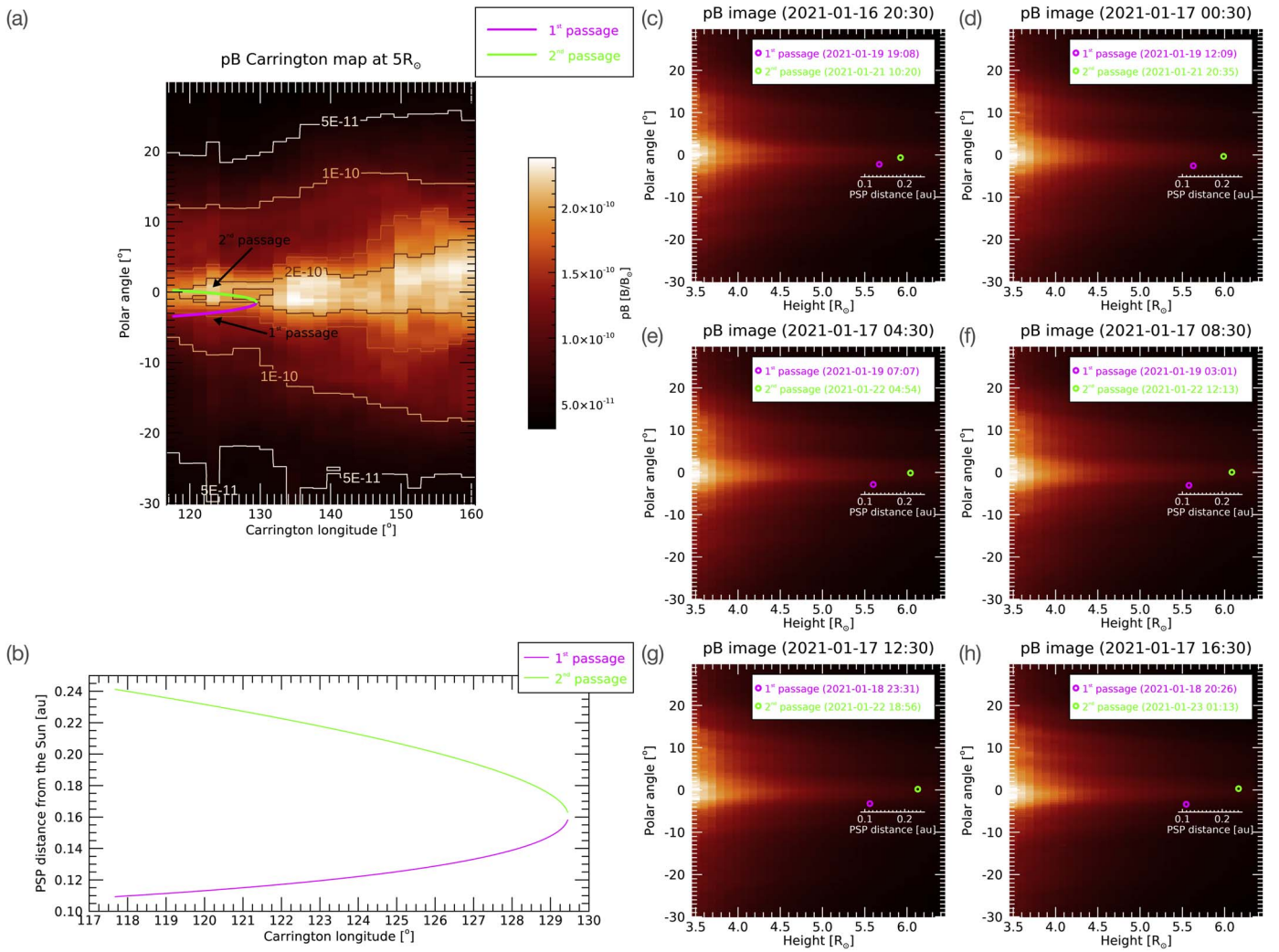


Figure 1. Overview of the joint SO/Metis—PSP observations. (a) Carrington map at $5R_{\odot}$ from Metis pB observations for the eastern solar limb on which is superimposed the back-projected trajectory of PSP during the first (magenta) and second (lime) passage (also labeled). (b) PSP distance as a function of Carrington longitude in the first (magenta) and second (lime) crossing of the same POS observed by Metis. (c)–(h) Expanded images of the FOV observed by Metis above the East limb of the Sun in the last six images acquired by the coronagraph; the apparent position of PSP during the Metis POS crossing is marked by an open circle (the color code is the same as the previous panels); the times at which the crossings occur are also reported in the legend; the extra white x-axis indicates the actual distance of PSP from the Sun.

Sorriso-Valvo et al. 2019) and deflect the magnetic field (possibly in association with switchback formation, Ruffolo et al. 2020) through the Kelvin–Helmholtz (KH) instability. Even without invoking KH-driven magnetic fluctuations, the small-scale flux ropes disconnected from the CS by magnetic reconnection enhance the amplitude of the quasi-2D MHD turbulence (Zank et al. 2018, 2020).

In order to clarify the correlation between the PSP measurements and the different regions of the CS crossed by the spacecraft, to provide additional information, such as the extent of the CS layers, and to support/complement the results outlined by Figure 2, Figures 3(a)–(d) show profiles of solar wind speed V , magnetic-field magnitude B normalized to the square of the distance r from the Sun,²⁸ angle between magnetic-field vector and radial direction θ_{RB} , and proton

plasma β_{\parallel} , as a function of the Carrington longitude range observed in conjunction by PSP and Metis.

As mentioned above, the boundaries of the CS were identified as the regions around the magnetic-field reversal. More specifically, Figure 3(c) clearly shows that during the first PSP passage, the magnetic field is directed toward the Sun out to $\sim 126^{\circ}$ Carrington longitude ($\theta_{RB} \sim 180^{\circ}$). Therefrom, the magnetic field shows no definite direction, fluctuating from inward ($\theta_{RB} \sim 180^{\circ}$) to outward ($\theta_{RB} \sim 0^{\circ}$) orientation. This is the region of the CS layer. Similarly, during the second PSP passage, from an initial positive polarity ($\theta_{RB} \sim 0^{\circ}$), the magnetic field changes direction for Carrington longitudes less than $\sim 119^{\circ}$, thereby identifying the second CS layer. It appears evident that at the edges of the CS (marked by dashed horizontal lines in the panels of Figure 3), the plasma speed, while remaining slow, undergoes moderate acceleration (Figure 3(a)), albeit more pronounced during the second crossing (lime line). This might be indicative of the presence of velocity shears that could explain the onset of greater

²⁸ Since $\nabla \cdot \mathbf{B} = 0$ the radial component of the magnetic field, B_R , clearly scales as r^2 and, as long as B_R is the dominant contributor to B -magnitude as during these observations, so does B .

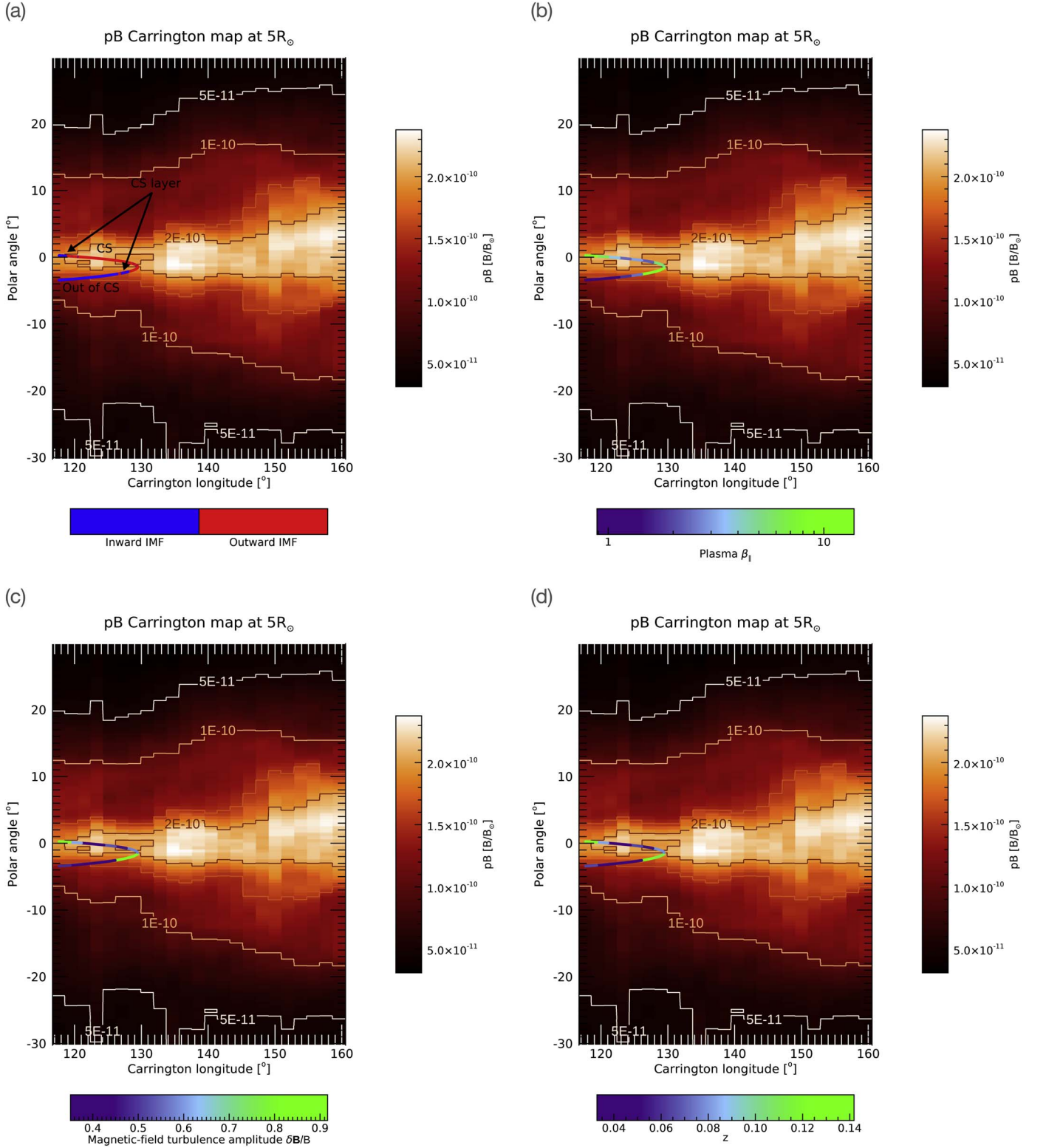


Figure 2. Projection onto the Metis pB Carrington map of (a) the IMF direction, (b) proton plasma β_{\parallel} , (c) magnetic-field turbulence amplitude $\delta B / \langle B \rangle$, and (d) magnetic-field deflection z (d), estimated from PSP measurements. The topology of the CS as flown through by PSP is outlined in (a).

turbulence at the CS boundaries. The latter is evident from the larger amplitude of B fluctuations (Figure 3(b)) as well as the more intense and numerous magnetic-field deflections, shown by the larger fluctuations of the B inclination with respect to the sampling direction. Finally, based on the aforementioned proposed mechanisms, the plasma β_{\parallel} also increases

significantly at the CS layers (Figure 3(d)). In addition to helping identify the different portions of the CS, the longitudinal series also allow for a more accurate estimate of the longitudinal extent of its boundaries, which turns out to be $3^{\circ}35'$ and $1^{\circ}67'$ wide during the first and second crossing, respectively.

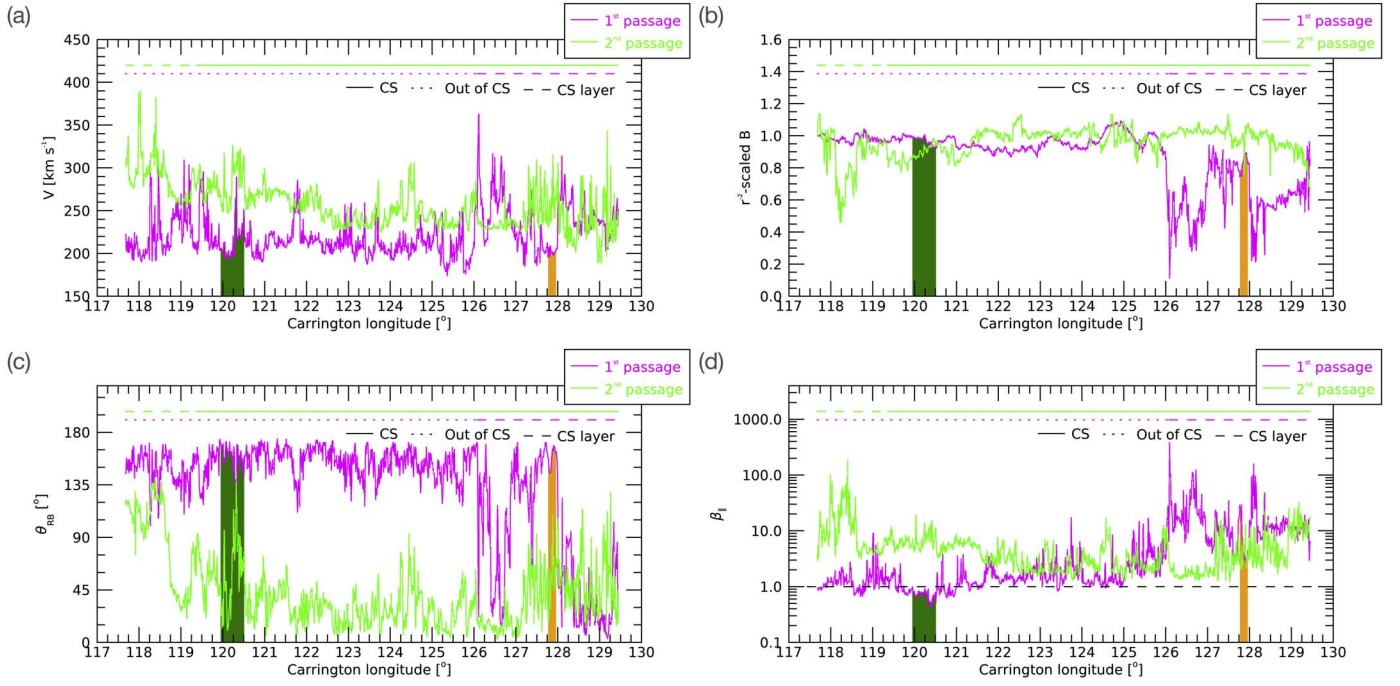


Figure 3. Measurements of (a) flow speed V , (b) r^2 -scaled magnetic-field intensity, (c) magnetic field radial direction angle θ_{RB} , and (d) proton plasma $\beta_{||}$ against Carrington longitude, during the first (magenta) and second (lime) PSP passage through the POS observed by Metis. Horizontal lines with different styles schematically depict the topology of the CS crossed by PSP. The green (orange) shaded area denotes an interval outside (at the edge) of the CS analyzed in Section 4.

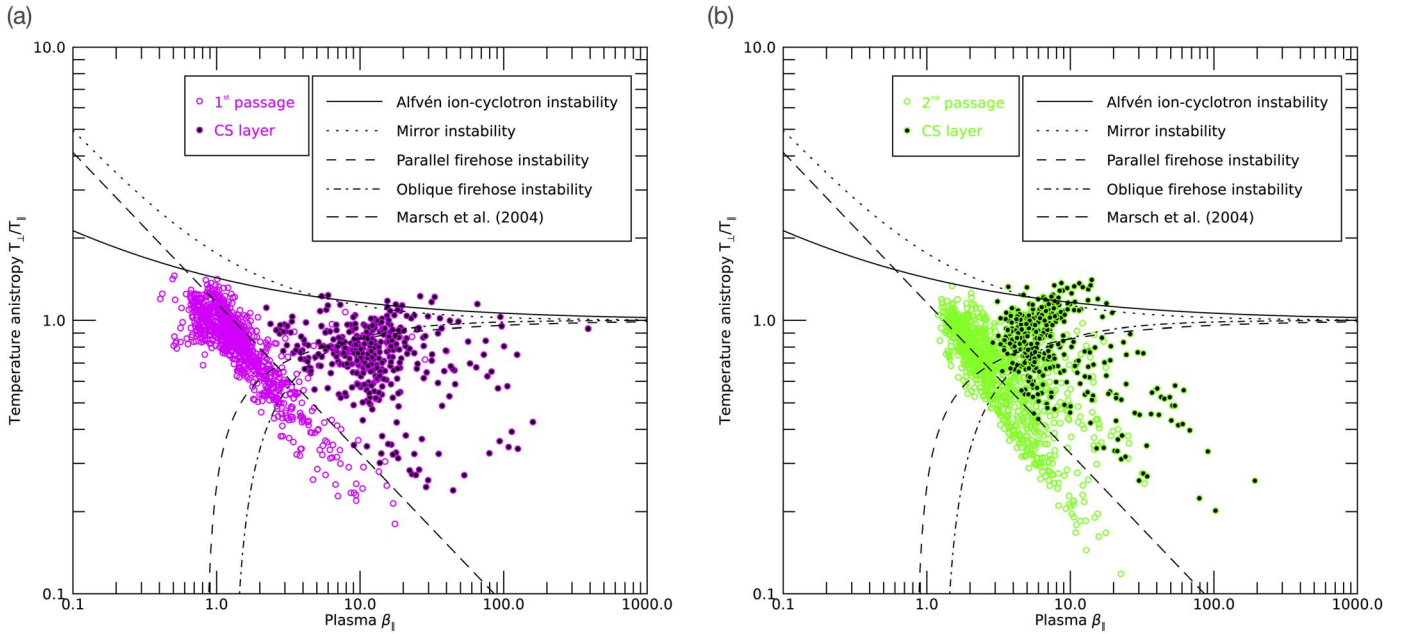


Figure 4. Scatterplot of the PSP observations in the $\beta_{||}$ - $T_{\perp}/T_{||}$ plane during the (a) first and (b) second PSP passage through the POS observed by Metis. The Alfvén ion cyclotron, mirror-mode, parallel and oblique firehose instability threshold curves are displayed as solid, dotted, dashed, and dashed-dotted lines, respectively. The empirical inverse relation by Marsch et al. (2004) is also shown as a long-dashed line. Black filled symbols refer to regions at the edges of the CS.

4. Onset of ICWs along the Turbulent CS

In order to assess whether the increase in turbulence occurring in the plasma across the CS affects the kinetic properties of the particle velocity distribution functions, especially regarding the nature of unstable wave-particle interactions, PSP measurements are plotted in the $\beta_{||}$ - $T_{\perp}/T_{||}$ plane (where $T_{\perp}/T_{||}$ is the temperature anisotropy) in Figure 4. The distribution is compared with different plasma instability thresholds (marked with different line types) as estimated by

Hellinger et al. (2006) for a maximum growth rate $\gamma = 10^{-3}\Omega_p$, where Ω_p is the proton gyro-frequency (see also the comprehensive review by Verscharen et al. 2019 and references therein).

When separating the data points based on the different portions of the CS crossed by PSP as identified in Figures 2 and 3, two different populations are distinguishable (though, less evident during the second passage). When inside or outside the CS (open symbols) PSP data distribute fairly well along the

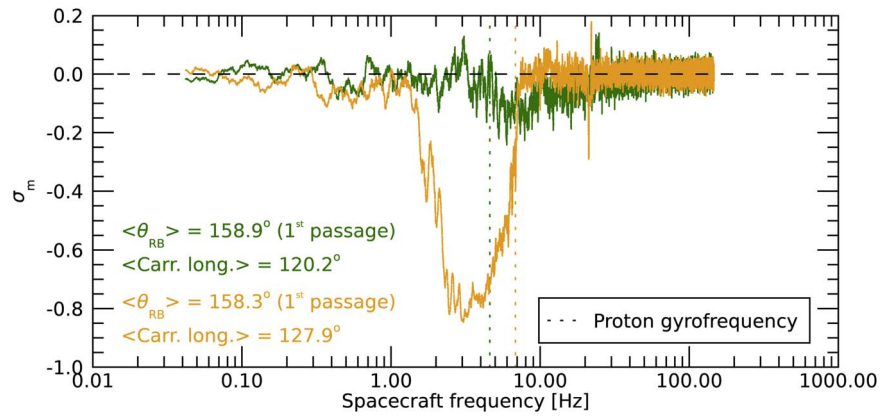


Figure 5. Magnetic helicity σ_m spectra computed outside (green) and along (orange) the CS when PSP was sampling the nearly parallel solar-wind magnetic field marked by same-color shaded regions in Figure 3. The corresponding local proton gyro-frequencies Ω_p are indicated by color-coded vertical dotted lines. The average Carrington longitude and sampling angle during both observations are also reported.

empirical anticorrelation curve found by Marsch et al. (2004) with Helios measurements (long-dashed line in Figure 4). Observations corresponding to the CS layers (black filled symbols) are instead mainly located at larger plasma β_{\parallel} . All instability thresholds shown in Figure 4 decrease with increasing β_{\parallel} . Therefore, the distribution of the CS layer data lies closer to the unstable regions of parameter space. Indeed, a significant portion of the parameter values computed from the data collected during the second CS crossing (Figure 4(b)) extends beyond the thresholds. As a result, the plasma along the CS is more likely to be disequibrated and thus trigger wave-particle instabilities. Therefore, it can be argued that the increased turbulence experienced at the CS boundaries, due to either magnetic reconnection-driven 2D flux ropes (Zhao et al. 2020, 2021) or KH fluctuations (Telloni et al. 2022a) that indirectly trigger the Alfvén ion cyclotron and the firehose instability via changes of the particle distributions. These instabilities then transfer energy from the particles (and thus restore a Maxwellian equilibrium condition) to the electromagnetic fields, i.e., generating ICWs and fast-mode waves (e.g., Sorriso-Valvo et al. 2019).

The presence of modes driven by temperature-anisotropy instabilities can, in principle, be inferred by identifying in space plasmas the corresponding polarization properties at the characteristic frequencies. Specifically, the presence of left-handed circularly polarized ICWs, which result from the Alfvén ion cyclotron instability, can be indicated through a strong peak in the normalized magnetic helicity σ_m spectrum near the local proton gyro-frequency (the magnetic helicity can indeed be used to diagnose the wave polarization state, Matthaeus & Goldstein 1982; Matthaeus et al. 1982). Moreover, the deeper and wider the helicity peak, the more numerous are the waves (Telloni et al. 2019). Searching for ICWs in the solar wind is, however, tricky. These are indeed waves with a wavevector parallel to the magnetic field. This means that any spacecraft can detect this kind of wave only when sampling solar wind plasma parallel to the mean magnetic field. One-hour intervals were then selected, inside, outside, and along the CS, where the σ_m spectrum was calculated, looking for significant peaks around Ω_p . It transpires that, on average, ICWs are prevalent at the edges of the CS, but are relatively scarce (about 50% less abundant) inside or outside the CS. Examples are given in Figure 5, where the σ_m spectra obtained in 1 hr intervals, nearly parallel to the

magnetic field, outside the CS (green) and along its boundaries (orange), during the first PSP trajectory, are shown. These intervals are indicated by shaded areas (with the same color code) in the longitude series in Figure 3. Note that because the spacecraft orbital velocity is greater during the first passage (PSP is closer to the Sun) the range of longitudes spanned in an hour is larger.

Although it should be mentioned that a higher Alfvénic contribution at fluid scales can also lead to the onset of ICWs (the reader is referred, in this regard, to Bruno & Telloni 2015; Telloni et al. 2019) even far from the CS, the analysis reported here suggests that instabilities, including the ICWs as shown in the example of Figure 5, are driven along the CS, where turbulent phenomena, related to either KH instability or magnetic disconnection processes, are most intense.

A large fraction of the data points lie above the thresholds for the firehose instabilities (dashed and dashed-dotted lines, respectively, in Figure 4). Although this applies both inside and outside the CS, it occurs mainly along the CS boundaries (only the core population at the CS layers exceeds the firehose instability; this is more evident during the first passage). In these time intervals, the system can drive parallel fast-mode waves with a polarization opposite from ICWs in the plasma frame (Woodham et al. 2021). A further in situ analysis of these fast-mode waves, however, is beyond the scope of the present work though, which focuses primarily on ICWs, whose presence is evidenced by Figure 5 and whose importance is related to their possible contribution in the coronal plasma heating mechanisms discussed in Section 1.

5. Concluding Remarks

The linkage of the temporal pattern of the increased turbulence and ICW burst with the spatial topology of the coronal structures documented in Figures 1–5 suggests this possible scenario. The large-scale CS layers are source regions of turbulence (via either KH instability or magnetic reconnection-driven 2D flux ropes), which pushes the plasma above the thresholds of instabilities, which in turn drive small-scale fluctuations/waves and regulate the plasma. Obviously, these effects are very strong near the Sun, where this is therefore a very efficient reshuffling of energy. Moreover, the correlation between the increased turbulence and ion cyclotron modes is important for connecting turbulence directly to heating. By estimating the turbulence energy per volume and adding up the

energy in the ion cyclotron modes per unit volume and further assuming this is dissipated (at a later time) over an ion inertial timescale, it would indeed be possible to obtain the heating rate and estimate the expected temperature. Theoretical work is currently in progress to test whether the energy released by turbulence and ICWs is sufficient to heat the plasma to temperatures of a million degrees and accelerate the slow solar wind along the CS. In addition, it would be worthwhile to undertake a more comprehensive statistical study of the occurrence of small-scale fluctuations inside and outside observed CS layers to obtain a better understanding of the universality of the proposed scenario. It is finally worth noting that the present results show a link between increased turbulence along the CS layers and the onset of temperature-anisotropy-driven instabilities, without however proving (but only suggesting) a cause-and-effect relationship. Causality between increased levels of turbulence and an increased strength of nonequilibrium plasma features could only be evidenced through statistical work and a nonlinear treatment of the turbulence–plasma interactions, which is left for future work.

This result shows the tremendous science potential of the Metis coronagraph on board SO, especially in conjunction with PSP. Indeed, the need for comparing/combining remote observations of the extended corona with local measurements of the solar wind acquired by different spacecraft (in quadrature) emerges clearly, not only to understand how large-scale coronal dynamics drives the onset of turbulence, waves, and kinetic instabilities, but also to develop simulation-based numerical experiments and/or theoretical models that can tackle long-lasting questions such as the coronal heating and wind acceleration problem.

Solar Orbiter is a space mission of international collaboration between ESA and NASA, operated by ESA. D.T. was partially supported by the Italian Space Agency (ASI) under contract 2018-30-HH.0. G.P.Z., L.A., and L.-L.Z. acknowledge the partial support of a NASA Parker Solar Probe contract SV4-84017, an NSF EPSCoR RII-Track-1 Cooperative Agreement OIA-2148653, and a NASA IMAP grant through SUB000313/80GSFC19C0027. L.S.-V. was funded by the SNSA grants 86/20 and 145/18. D.V. is supported by STFC Ernest Rutherford Fellowship ST/P003826/1 and STFC Consolidated Grants ST/S000240/1 and ST/W001004/1. The Metis program is supported by ASI under contracts to the National Institute for Astrophysics and industrial partners. Metis was built with hardware contributions from Germany (Bundesministerium für Wirtschaft und Energie through the Deutsches Zentrum für Luft- und Raumfahrt e.V.), the Czech Republic (PRODEX), and ESA. The Metis data analyzed in this paper are available from the PI on request. Parker Solar Probe data was downloaded from the NASA’s Space Physics Data Facility (<https://spdf.gsfc.nasa.gov>). This work was discussed at the ISSI Team “Ion Kinetic Instabilities in the Solar Wind in Light of Parker Solar Probe and Solar Orbiter Observations” led by L. Ofman and L. Jian.

ORCID iDs

Daniele Telloni  <https://orcid.org/0000-0002-6710-8142>
 Gary P. Zank  <https://orcid.org/0000-0002-4642-6192>
 Laxman Adhikari  <https://orcid.org/0000-0003-1549-5256>
 Lingling Zhao  <https://orcid.org/0000-0002-4299-0490>

Roberto Susino  <https://orcid.org/0000-0002-1017-7163>
 Ester Antonucci  <https://orcid.org/0000-0003-4155-6542>
 Silvano Fineschi  <https://orcid.org/0000-0002-2789-816X>
 Marco Stangalini  <https://orcid.org/0000-0002-5365-7546>
 Catia Grimani  <https://orcid.org/0000-0002-5467-6386>
 Luca Sorriso-Valvo  <https://orcid.org/0000-0002-5981-7758>
 Daniel Verscharen  <https://orcid.org/0000-0002-0497-1096>
 Raffaele Marino  <https://orcid.org/0000-0002-6433-7767>
 Silvio Giordano  <https://orcid.org/0000-0002-3468-8566>
 Raffaella D’Amicis  <https://orcid.org/0000-0003-2647-117X>
 Denise Perrone  <https://orcid.org/0000-0003-1059-4853>
 Francesco Carbone  <https://orcid.org/0000-0002-3559-5273>
 Alessandro Liberatore  <https://orcid.org/0000-0002-0016-7594>
 Roberto Bruno  <https://orcid.org/0000-0002-2152-0115>
 Gaetano Zimbardo  <https://orcid.org/0000-0002-9207-2647>
 Marco Romoli  <https://orcid.org/0000-0001-9921-1198>
 Vincenzo Andretta  <https://orcid.org/0000-0003-1962-9741>
 Vania Da Deppo  <https://orcid.org/0000-0001-6273-8738>
 Petr Heinzel  <https://orcid.org/0000-0002-5778-2600>
 John D. Moses  <https://orcid.org/0000-0001-9670-2063>
 Giampiero Naletto  <https://orcid.org/0000-0003-2007-3138>
 Gianalfredo Nicolini  <https://orcid.org/0000-0002-9459-3841>
 Daniele Spadaro  <https://orcid.org/0000-0003-3517-8688>
 Luca Teriaca  <https://orcid.org/0000-0001-7298-2320>
 Aleksandr Burtovoi  <https://orcid.org/0000-0002-8734-808X>
 Yara De Leo  <https://orcid.org/0000-0003-2426-2112>
 Giovanna Jerse  <https://orcid.org/0000-0002-0764-7929>
 Federico Landini  <https://orcid.org/0000-0001-8244-9749>
 Maurizio Pancrazzi  <https://orcid.org/0000-0002-3789-2482>
 Clementina Sasso  <https://orcid.org/0000-0002-5163-5837>
 Alessandra Slemmer  <https://orcid.org/0000-0001-7762-280X>

References

- Adhikari, L., Zank, G. P., Telloni, D., & Zhao, L.-L. 2022, *ApJL*, 937, L29
 Adhikari, L., Zank, G. P., & Zhao, L. L. 2020a, *ApJ*, 901, 102
 Adhikari, L., Zank, G. P., Zhao, L. L., Nakanotani, M., & Tasnim, S. 2021, *A&A*, 650, A16
 Adhikari, L., Zank, G. P., Zhao, L. L., et al. 2020b, *ApJS*, 246, 38
 Alexandrova, O., Chen, C. H. K., Sorriso-Valvo, L., Horbury, T. S., & Bale, S. D. 2013, *SSRv*, 178, 101
 Antonucci, E., Downs, C., Capuano, G. E., et al. 2023, PhFI, in press
 Antonucci, E., Harra, L., Susino, R., & Telloni, D. 2020a, *SSRv*, 216, 117
 Antonucci, E., Romoli, M., Andretta, V., et al. 2020b, *A&A*, 642, A10
 Bale, S. D., Goetz, K., Harvey, P. R., et al. 2016, *SSRv*, 204, 49
 Bale, S. D., Kasper, J. C., Howes, G. G., et al. 2009, *PhRvL*, 103, 211101
 Bale, S. D., Kellogg, P. J., Mozer, F. S., Horbury, T. S., & Reme, H. 2005, *PhRvL*, 94, 215002
 Bandyopadhyay, R., Matthaeus, W. H., McComas, D. J., et al. 2022, *ApJL*, 926, L1
 Bowen, T. A., Chandran, B. D. G., Squire, J., et al. 2022, *PhRvL*, 129, 165101
 Bruno, R., & Carbone, V. 2013, *LRSP*, 10, 2
 Bruno, R., & Telloni, D. 2015, *ApJL*, 811, L17
 Bruno, R., & Trenchi, L. 2014, *ApJL*, 787, L24
 Carbone, V., Telloni, D., Lepreti, F., & Vecchio, A. 2022, *ApJL*, 924, L26
 Chandran, B. D. G., Li, B., Rogers, B. N., Quataert, E., & Germaschewski, K. 2010, *ApJ*, 720, 503
 Chen, C. H. K., Chandran, B. D. G., Woodham, L. D., et al. 2021, *A&A*, 650, L3
 Chen, C. H. K., Klein, K. G., & Howes, G. G. 2019, *NatCo*, 10, 740
 Cranmer, S. R. 2000, *ApJ*, 532, 1197
 Cranmer, S. R., Field, G. B., & Kohl, J. L. 1999a, *ApJ*, 518, 937
 Cranmer, S. R., Kohl, J. L., Noci, G., et al. 1999b, *ApJ*, 511, 481
 De Leo, Y., Burtovoi, A., Teriaca, L., et al. 2023, *A&A*, in press

- Domingo, V., Fleck, B., & Poland, A. I. 1995, *SoPh*, **162**, 1
- Dudok de Wit, T., Krasnoselskikh, V. V., Bale, S. D., et al. 2020, *ApJS*, **246**, 39
- Fineschi, S., Naletto, G., Romoli, M., et al. 2020, *ExA*, **49**, 239
- Fox, N. J., Velli, M. C., Bale, S. D., et al. 2016, *SSRv*, **204**, 7
- He, J., Marsch, E., Tu, C., Yao, S., & Tian, H. 2011, *ApJ*, **731**, 85
- Hellinger, P., Trávníček, P., Kasper, J. C., & Lazarus, A. J. 2006, *GeoRL*, **33**, L09101
- Hollweg, J. V., & Isenberg, P. A. 2002, *JGRA*, **107**, 1147
- Howes, G. G., Dorland, W., Cowley, S. C., et al. 2008, *PhRvL*, **100**, 065004
- Howes, G. G., McCubbin, A. J., & Klein, K. G. 2018, *JPIPh*, **84**, 905840105
- Hundhausen, A. J. 1972, *Coronal Expansion and Solar Wind* (Berlin: Springer)
- Kasper, J. C., Abiad, R., Austin, G., et al. 2016, *SSRv*, **204**, 131
- Kasper, J. C., Klein, K. G., Lichko, E., et al. 2021, *PhRvL*, **127**, 255101
- Kohl, J. L., Esser, R., Gardner, L. D., et al. 1995, *SoPh*, **162**, 313
- Kohl, J. L., Noci, G., Antonucci, E., et al. 1998, *ApJL*, **501**, L127
- Leamon, R. J., Matthaeus, W. H., Smith, C. W., & Wong, H. K. 1998, *ApJL*, **507**, L181
- Leamon, R. J., Matthaeus, W. H., Smith, C. W., et al. 2000, *ApJ*, **537**, 1054
- Li, X., Habbal, S. R., Hollweg, J. V., & Esser, R. 1999, *JGRA*, **104**, 2521
- Luo, Q., Zhu, X., He, J., et al. 2022, *ApJ*, **928**, 36
- Mandrini, C. H., Démoulin, P., & Klimchuk, J. A. 2000, *ApJ*, **530**, 999
- Marino, R., & Sorriso-Valvo, L. 2023, *PhR*, **1006**, 1
- Marsch, E., Ao, X. Z., & Tu, C. Y. 2004, *JGRA*, **109**, A04102
- Martinović, M. M., Klein, K. G., Kasper, J. C., et al. 2020, *ApJS*, **246**, 30
- Matthaeus, W. H., & Goldstein, M. L. 1982, *JGRA*, **87**, 10347
- Matthaeus, W. H., Goldstein, M. L., & Smith, C. 1982, *PhRvL*, **48**, 1256
- Matthaeus, W. H., Zank, G. P., Oughton, S., Mullan, D. J., & Dmitruk, P. 1999, *ApJL*, **523**, L93
- Müller, D., St. Cyr, O. C., Zouganelis, I., et al. 2020, *A&A*, **642**, A1
- Parker, E. N. 1972, *ApJ*, **174**, 499
- Phan, T. D., Verniero, J. L., Larson, D., et al. 2022, *GeoRL*, **49**, e96986
- Podesta, J. J., & Gary, S. P. 2011, *ApJ*, **734**, 15
- Priest, E. R. 1985, *RPPH*, **48**, 955
- Réville, V., Fargette, N., Rouillard, A. P., et al. 2022, *A&A*, **659**, A110
- Ruffolo, D., Matthaeus, W. H., Chhiber, R., et al. 2020, *ApJ*, **902**, 94
- Sahraoui, F., Goldstein, M. L., Belmont, G., Canu, P., & Rezeau, L. 2010, *PhRvL*, **105**, 131101
- Shi, C., Velli, M., Panasenco, O., et al. 2021, *A&A*, **650**, A21
- Shi, C., Velli, M., Tenerani, A., Réville, V., & Rappazzo, F. 2022, *ApJ*, **928**, 93
- Sorriso-Valvo, L., Catapano, F., Retinò, A., et al. 2019, *PhRvL*, **122**, 035102
- Stawarz, J. E., Eriksson, S., Wilder, F. D., et al. 2016, *JGRA*, **121**, 021
- Telloni, D., Adhikari, L., Zank, G. P., et al. 2022a, *ApJ*, **929**, 98
- Telloni, D., Adhikari, L., Zank, G. P., et al. 2022b, *ApJL*, **938**, L8
- Telloni, D., Andretta, V., Antonucci, E., et al. 2021, *ApJL*, **920**, L14
- Telloni, D., Antonucci, E., & Doderò, M. A. 2007a, *A&A*, **472**, 299
- Telloni, D., Antonucci, E., & Doderò, M. A. 2007b, *A&A*, **476**, 1341
- Telloni, D., & Bruno, R. 2016, *MNRAS: Lett.*, **463**, L79
- Telloni, D., Bruno, R., & Trenchi, L. 2015, *ApJ*, **805**, 46
- Telloni, D., Carbone, F., Bruno, R., et al. 2019, *ApJL*, **885**, L5
- Telloni, D., Zank, G. P., Sorriso-Valvo, L., et al. 2022c, *ApJ*, **935**, 112
- Verdini, A., Velli, M., & Buchlin, E. 2009, *ApJL*, **700**, L39
- Verdini, A., Velli, M., Matthaeus, W. H., Oughton, S., & Dmitruk, P. 2010, *ApJL*, **708**, L116
- Verneta, A. I., Antonucci, E., & Marocchi, D. 1994, *SSRv*, **70**, 299
- Verscharen, D., Klein, K. G., & Maruca, B. A. 2019, *LRSP*, **16**, 5
- Woodham, L. D., Wicks, R. T., Verscharen, D., TenBarge, J. M., & Howes, G. G. 2021, *ApJ*, **912**, 101
- Woodham, L. D., Wicks, R. T., Verscharen, D., et al. 2019, *ApJL*, **884**, L53
- Zank, G. P., Adhikari, L., Hunana, P., et al. 2017, *ApJ*, **835**, 147
- Zank, G. P., Adhikari, L., Hunana, P., et al. 2018, *ApJ*, **854**, 32
- Zank, G. P., Nakanotani, M., Zhao, L.-L., Adhikari, L., & Telloni, D. 2020, *ApJ*, **900**, 115
- Zank, G. P., Zhao, L. L., Adhikari, L., et al. 2021, *PhPI*, **28**, 080501
- Zank, G. P., Zhao, L. L., Adhikari, L., et al. 2022, *ApJL*, **926**, L16
- Zhao, L. L., Zank, G. P., Adhikari, L., et al. 2020, *ApJS*, **246**, 26
- Zhao, L. L., Zank, G. P., Adhikari, L., et al. 2022, *ApJL*, **934**, L36
- Zhao, L. L., Zank, G. P., Hu, Q., et al. 2021, *A&A*, **650**, A12
- Zirker, J. B. 1993, *SoPh*, **148**, 43